INTERNATIONAL JOURNAL FOR NUMERICAL METHODS IN FLUIDS
Int. J. Numer. Meth. Fluids **28**: 419–442 (1998)

DESIGN SENSITIVITY AND FINITE ELEMENT ANALYSIS OF FREE SURFACE FLOWS WITH APPLICATION TO OPTIMAL DESIGN OF CASTING RIGGING SYSTEMS

ROBERT M. MCDAVID AND JONATHAN A. DANTZIG*

Department of Mechanical and Industrial Engineering, University of Illinois at Urbana-Champaign, Urbana, IL 61801, USA

SUMMARY

A novel, fully-analytical design sensitivity formulation for transient, turbulent, free surface flows is derived and implemented in the context of finite element analysis. The time-averaged, turbulent form of the Navier–Stokes equations are solved using a mixing length model, in conjunction with the volume of fluid (VOF) method to model the free surface movement. The design derivatives of these governing equations are computed and solved to find the analytical sensitivities of the fluid position, velocity and pressure fields with respect to shape design variables. The computational efficiency produced by evaluating the sensitivities analytically is demonstrated. The design of the runner and gating system of a simple block casting is presented as an example application for using sensitivity information in design. The analytical sensitivity routine is coupled to a numerical optimizer to yield an automated method for optimal design of the casting rigging system. The results produce runner shapes which eliminate mold-gas aspiration. © 1998 John Wiley & Sons, Ltd.

KEY WORDS: finite element analysis; design sensitivity analysis; optimization; mold filling; free surface; turbulence

1. INTRODUCTION

Sand casting is an example of a material processing operation involving free-surface fluid flow. Molten material is poured into a shaped cavity (mold), via a delivery system of ducts and channels, with the fluid displacing the air within. Figure 1 shows a typical arrangement of components in a sand casting mold. The shape, size and placement of the sprue, runners and ingates are critical to the entire process, because they determine, among other things, the rate, uniformity and smoothness with which material is delivered to the mold cavity. The volume of material in the rigging system also represents additional cost in the process. The uniformity and smoothness of the material delivery have important implications for the quality of the final part. Therefore, the design of the rigging system to achieve quality and production goals is of prime importance.

Traditionally, runner and gating systems for foundry castings have been designed using generic design rules, such as those compiled by the American Foundryman's Society [1]. Originally developed five decades ago, these rules provide guidelines for the sizing of sprues, runners and gates. The objective of these designs is to provide smooth, non-agitated delivery

* Correspondence to: Department of Mechanical and Industrial Engineering, University of Illinois at Urbana-Champaign, 1206 West Green Street, Urbana, IL 61801, USA

CCC 0271–2091/98/130419–24$17.50

Received June 1997
Revised October 1997

of metal into the mold, while avoiding defects due to events such as premature solidification and gas aspiration in the runners. The design rules currently used are based primarily on Bernoulli's equation, along with empirical data [2,3] gathered using simple shapes. While these rules produce satisfactory results for many castings, more complex castings lead to many, and sometimes conflicting requirements to provide a sound casting. Computer simulation and modeling can provide valuable insight into rigging system design for these demanding applications.

The volume of fluid (VOF) method [4] has made it computationally feasible to model mold filling in realistic geometries, because of its ability to accommodate the large surface deformations commonly encountered in mold filling. This is in contrast to deformable grid techniques [5,6] for simulating free-surface flows, which perform best when free-surface movements are relatively limited.

The filling process can sometimes be modeled, assuming that the flow is inviscid and irrotational [7]. In this case, the VOF equation can be used in conjunction with Bernoulli's equation to simulate mold filling. Although this formulation has the advantage of being less computationally intensive than solving the full Navier–Stokes equations, numerical and physical modeling studies [8,9] have shown that viscous effects cannot be neglected in many castings. At the large Reynolds numbers encountered in metal casting, the flow can be assumed to be inviscid in the core. However, near the walls of the metal delivery system, viscous effects predominate. Since defects due to mold erosion, gas aspiration, turbulent eddy formation and other phenomena are correlated to the processes occurring at the wall, it seems likely that inviscid calculations will fail to correctly predict these effects.

Design of a successful rigging system requires consideration of a number of competing phenomena. For example, although rapid filling of the mold is desirable, it is constrained by the need to avoid agitation of the metal flow and mold erosion. The latter has been correlated with the shear strength of the sand and the liquid metal velocity [10].

Avoiding agitation of the metal stream is another primary goal of runner design, because of the many potential problems that can otherwise occur. For example, agitation can cause surface oxides to be entrained. Entrained oxides in the casting reduce both fatigue and ultimate strength. This problem is of particular importance in aluminum alloy casting [1].

The formation of vortices and eddies can both lead to an agitated flow stream. In regions of low pressure, air and mold gases can be aspirated into the metal stream from the mold itself. This is the reason that, e.g. the sprue is tapered. Similarly, the sprue should have a square cross-section to suppress the formation of vortices.

We may summarize these statements and a few other rules as objectives and constraints:

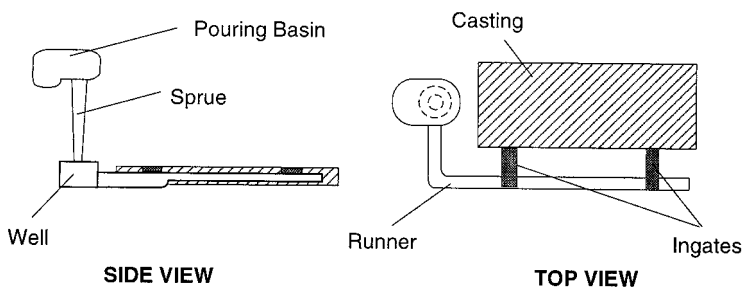

Figure 1. Schematic diagram showing components of a typical sand casting.

1. Maximize casting yield by reducing total gating system volume
2. Minimize mold and core erosion
3. Minimize agitation of metal stream
4. Minimize vortex and eddy formation in rigging system

It is a challenging problem to determine the shapes of the runners, sprues and ingates to fill the mold quickly, while satisfying constraints on overall size and mold erosion. Clearly, it is not always possible to accomplish this either intuitively or by applying rules derived for simple shapes, and much trial and error is still necessary. One objective of this work is to develop a new, more direct method for casting-rigging design. The design of the delivery system is treated as an optimization problem, wherein a systematic method for optimally sizing the runners and ingates is applied. This method requires an efficient means for computing the sensitivities of the free surface flow with respect to the design parameters describing the runner and ingate shapes. By coupling this sensitivity information with a gradient-based numerical optimization algorithm, an automated system for casting rigging design is possible. Bradley [11] suggested a similar approach, using simple hydraulic models to model mold filling, although, to our knowledge, this technique was never implemented.

The key component in this design system is the ability to compute the flow and its sensitivity to various design parameters. Analytical methods for computing the design sensitivities, by solving the design derivatives of the governing finite element equations, have been successfully applied in past work. In particular, this method has found widespread application in the field of structural mechanics. Significant contributions have been made in the areas of sensitivity analysis for non-linear structural mechanics [12,13], vibration control [14,15], and geometrically non-linear systems [16] to name a few. Additionally, sensitivity methods have been formulated for linear [17–19] and non-linear [20,21] thermal systems. Furthermore, previous researchers have developed semi-analytical [22,23] and fully-analytical [24] methods for computing flow sensitivities without free surfaces [24].

In this work, analytical sensitivity analysis methods have been developed for mold filling applications. Based on the preceding discussion, inclusion of viscous terms in near-wall regions is important. The VOF method, in conjunction with the Navier–Stokes equations, is chosen for modeling the free surface flow in mold filling. A mixing-length model is used for closure of the time-averaged Navier–Stokes equations, to account for turbulence effects. Expressions for the design derivatives of the finite element form of these models are developed and then implemented by modifying the commercial CFD code FIDAP™ [25]. This approach has been used successfully in the past to compute the sensitivities for steady, turbulent flows without filling [24], and for thermal problems involving solidification [26,27]. The optimal design of a rigging system for a simple block casting is then presented as an example using these newly developed algorithms.

2. MODEL FORMULATION

A mathematical model is constructed to simulate the transient, free-surface flow which occurs in casting mold filling. This model is formulated by solving the mass and momentum balance equations in a domain representing the casting mold using the finite element method. The sensitivities are subsequently evaluated by solving for the design derivatives of the discretized governing equations on the computational domain.

2.1. Mass, momentum and energy equations

The balance of mass, momentum and energy for an incompressible Newtonian fluid may be written as follows (see Appendix A for a list of symbols):

$$\nabla \cdot \mathbf{u} = 0, \tag{1}$$

$$\rho \left\{ \frac{\partial \mathbf{u}}{\partial t} + \mathbf{u} \cdot \nabla \mathbf{u} \right\} = -\nabla p + \nabla \cdot [\mu(\nabla \mathbf{u} + (\nabla \mathbf{u})^T)] + \rho \mathbf{g}, \tag{2}$$

where $\mathbf{u}$ is the continuum velocity vector, p is the continuum pressure, ρ is the fluid density, μ is the molecular viscosity of the fluid, and $\mathbf{g}$ is the bodyforce vector. Relevant dimensionless groups may be computed to assess the importance of various phenomena. We may compute a characteristic flow velocity (U_c) for the runner system by equating inertial and gravitational effects in the sprue (i.e. set the Froude number [28], $Fr = 1$). Assuming a sprue height (L) of 150 mm leads to a value of $U_c = 1200$ mm s^{-1}.

The relative importance of inertial to viscous forces in the flow is estimated from the characteristic Reynolds number ($Re = \rho U_c d/\mu$) based on the diameter at the sprue base (d) and U_c. For aluminum, $Re \approx 60000$, which indicates that the flow will be turbulent [28,29]. Similarly, the importance of surface tension is indicated by the Weber number (We [28]), which evaluates to 1000, indicating that surface tension may be neglected relative to inertia.

The flow may be considered to be isothermal during mold filling because the temperature change in the characteristic filling time does not cause a significant change in the viscosity of the liquid metal. As such, the temperature equation is uncoupled from the momentum equation. Also, the quantity of heat convected into the mold cavity compared with the heat loss by conduction to the sand, normal to the predominant flow direction, is estimated by the Graetz number ($Gz = U_c h/\alpha$). If h is the typical runner thickness, the Graetz number of 1000 indicates that heat is transported to the mold cavity faster than it can be lost by diffusion to the sand. Accordingly, the energy equation is neglected in this work.

To account for high Reynolds number effects, a mixing length turbulence model [29,30] is used. In this model, the turbulent component of viscosity μ_t is assumed to be related to the magnitude of the local shear rate through a mixing length, l_t:

$$\mu_t = \rho l_t^2 S, \tag{3}$$

where

$$S^2 = \dot{\boldsymbol{\gamma}} : \dot{\boldsymbol{\gamma}}, \tag{4}$$

where $\dot{\boldsymbol{\gamma}}$ is the strain-rate tensor. The mixing length hypothesis can be applied with great success for relatively simple flows [30]. In boundary layer flows, a ramp function for specifying the mixing length, such as that illustrated in Figure 2, has been found to be satisfactory [30]. The model has three parameters: δ, the distance from the wall to a point where the velocity is within 1% of the free stream velocity, and two empirical constants, $\kappa = 0.435$ and $\lambda = 0.09$, the values of which, for simple flows with limited swirl, were given by Patankar and Spalding [31].

2.2. VOF equation

The VOF method [4] is used to compute the location and movement of the fluid front. θ is an order parameter used to track the location of the flow front. Within the fluid θ has a value of unity, and outside the fluid θ is zero. θ is convected with the fluid, but not diffused, and therefore satisfies the equation

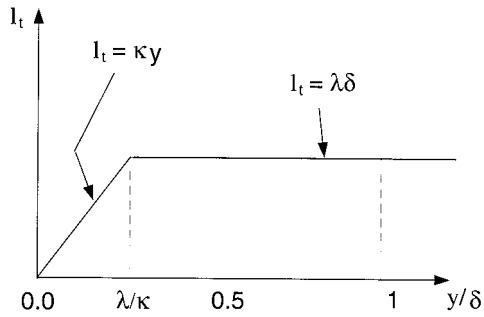

Figure 2. Mixing-length distribution in wall boundary layers.

$$\frac{\partial\theta}{\partial t} + \mathbf{u}\cdot\nabla\theta = 0. \tag{5}$$

Introducing such a form for θ can result in a diffuse interface, depending on the solution method. The VOF method is implemented in FIDAP [32] by enforcing Equation (5) on each element as a control volume. To perform volume tracking, the filling fraction in element i, $f_i \in [0, 1]$, is defined as

$$f_i = \frac{1}{V_i}\int_{V_i} \theta \, \mathrm{d}V_i, \tag{6}$$

where $f_i = 1$ denotes a full element, $f_i = 0$ an empty element, and fractional values denote partially filled elements. Performing a mass balance on an element produces an explicit evolution equation for the element fill state:

$$f_i^{n+1} = f_i^n + \left[\frac{\Delta t_{\text{fill}}}{V_i}\sum_k Q_{ik}^n\right], \tag{7}$$

where the superscripts refer to time steps, and Q_{ik}^n is the flow rate of fluid into element i, through face k at the nth time step. The flow rate Q_{ik}^n can be further expressed as the product of geometric and flow parameters, giving

$$Q_{ik}^n = -\alpha_{ik} q_k^n = -\alpha_{ik}\int_k \mathbf{u}^n\cdot\hat{n}\,\mathrm{d}\Omega, \tag{8}$$

where $\mathbf{u}^n$ is the velocity solution at the nth time step, and $\alpha_{ik} \in [0, 1]$ is a geometric factor representing the fraction of side k, in element i, across which fluid flows. α_{ik} is determined from the 'reconstruction' or spatial location of fluid in the mesh at time step n. This reconstruction is determined from the fill state for the element i, and the fill states of its neighboring elements. The reader is referred to the FIDAP v7.5 Update Manual [32] for an illustration of all the possible reconstructions for a quadrilateral element. These reconstruction rules can also be formulated for 3D cases. The underlying premise is that each case represents a unique filling situation, and the rules must be exhaustive.

Equation (7) does not guarantee that the filling fraction at the next time step, f_i^{n+1} will take on a value between 0 and 1. In this implementation, a 'flux-limiting' approach is used to ensure that elements are not over-filled or over-emptied. Depending on the fill states of neighboring elements and the value of a test quantity, the geometric factor α_{ik} is adjusted so that the exiting flux results in a fill fraction of exactly 0 or 1 in the extreme cases.

Finally, because an explicit scheme is used to compute the fill fraction, the filling time step size, Δt_{fill}, is limited by the Courant–Friedrichs–Lewy (CFL) condition [33] for numerical stability. The CFL condition is modified by selection of the Courant number $\Gamma < 1$, for non-linear, multi-dimensional problems, so that the maximum usable time step is given by

$$\Delta t_{\text{fill}} \leq \min_{i,k}\left(\frac{\Gamma V_i}{Q_{ik}^n}\right). \tag{9}$$

It should be noted that Δt_{fill} is proportional to the size of the elements (V_i). Equation (9) therefore ensures that the filling front does not advance by more than one element in one time step.

The time step used to integrate the Navier–Stokes equations, Δt_{flow} is selected to control the local time truncation error, and is dependent on the velocity solution at three time steps. If the maximum desirable truncation error is $\epsilon_{\Delta t}$, the time step size to be used for the next step is computed using

$$\Delta t_{\text{flow}}^n = \Delta t_{\text{flow}}^{n-1}\left[\frac{\epsilon_{\Delta t}}{\|d_n\|}\right]^{1/2}, \tag{10}$$

where $\|d_n\|$ is the estimate of the time truncation error at the current step. The reader is referred to the FIDAP Theoretical Manual for full details of the variable time step algorithm. However, it is clear that Δt_{fill} and Δt_{flow} may differ. If $\Delta t_{\text{fill}} < \Delta t_{\text{flow}}$, then several filling steps may be taken for each flow time step in a subcycling strategy. However, for our purposes, subcycling is not allowed. Instead, the minimum of Δt_{fill} and Δt_{flow} is used to integrate both the Navier–Stokes equations and the VOF filling equation. This procedure is adopted to eliminate the solution sensitivity dependence on the time step size.

2.3. Finite element discretization and solution

The Galerkin finite element method is used to solve the mass and momentum balance equations for the velocity and pressure fields. Applying this formulation converts the governing partial differential equations into a set of non-linear algebraic matrix equations. In two-dimensions, these governing finite element equations are

$$\mathbf{C}_i^T\mathbf{U}_i = 0, \tag{11}$$

$$\mathbf{M}\frac{\partial \mathbf{U}_1}{\partial t} + [\mathbf{A}_1(\mathbf{U}_1) + \mathbf{A}_1(\mathbf{U}_2)] + [2\mathbf{D}_{11} + \mathbf{D}_{22}]\mathbf{U}_1 + \mathbf{D}_{12}\mathbf{U}_2 - \mathbf{C}_1\mathbf{P} = \mathbf{F}_1, \tag{12}$$

$$\mathbf{M}\frac{\partial \mathbf{U}_2}{\partial t} + [\mathbf{A}_2(\mathbf{U}_1) + \mathbf{A}_2(\mathbf{U}_2)] + [\mathbf{D}_{11} + 2\mathbf{D}_{22}]\mathbf{U}_2 + \mathbf{D}_{21}\mathbf{U}_1 - \mathbf{C}_2\mathbf{P} = \mathbf{F}_2, \tag{13}$$

where $\mathbf{U}_i$ is the nodal solution vector for velocity in the i-direction, while $\mathbf{P}$ contains the nodal pressures. Note that the temperature degree of freedom and the energy equation are absent, because the mold filling is assumed to be isothermal. The various matrices and vectors in Equations (11)–(13) are evaluated through volume (V) and surface (Ω) integrals, as

$$\mathbf{C}_i = \int_V \rho \frac{\partial \boldsymbol{\phi}}{\partial x_i}\boldsymbol{\psi}^T \,\mathrm{d}V, \tag{14}$$

$$\mathbf{M} = \int_V \rho \boldsymbol{\phi}\boldsymbol{\phi}^T \,\mathrm{d}V, \tag{15}$$

$$\mathbf{A}_i(\mathbf{U}_j) = \int_V \rho \boldsymbol{\phi} u_j \frac{\partial \boldsymbol{\phi}^{\mathrm{T}}}{\partial x_j} \, \mathrm{d}V, \tag{16}$$

$$\mathbf{D}_{ij} = \int_V \mu \frac{\partial \boldsymbol{\phi}}{\partial x_j} \frac{\partial \boldsymbol{\phi}^T}{\partial x_i} \, \mathrm{d}V, \tag{17}$$

$$\mathbf{F}_i = \int_\Omega \sigma_i \boldsymbol{\phi} \, \mathrm{d}\Omega + \int_V \rho g_i \boldsymbol{\phi} \, \mathrm{d}V. \tag{18}$$

Here, σ_i denotes applied tractions resolved in the i-direction. $\boldsymbol{\phi}$ and $\boldsymbol{\psi}$ are vectors of the velocity and pressure basis functions, defined by

$$p = \boldsymbol{\psi} \cdot \mathbf{P}, \tag{19}$$

and

$$u_i = \boldsymbol{\phi} \cdot \mathbf{U}_i. \tag{20}$$

The velocity basis functions are chosen to be one-order higher polynomial interpolation than the pressure basis functions, to stabilize the solution scheme [34]. The reader is referred to standard finite element texts [35,36] for full details of this method.

When a suitable time-integration scheme is applied to Equations (11)–(13), the governing finite element equations may be written in an explicit form as

$$\mathbf{K}(\boldsymbol{\Psi}_j^{n+1}, \Delta t)\boldsymbol{\Psi}_j^{n+1} = \mathbf{F}(\boldsymbol{\Psi}^n, \Delta t), \tag{21}$$

where

$$\boldsymbol{\Psi}_j^{n+1} = \begin{Bmatrix} \mathbf{U}_{1j}^{n+1} \\ \mathbf{U}_{2j}^{n+1} \\ \mathbf{P}_j^{n+1} \end{Bmatrix}.$$

$\boldsymbol{\Psi}_j^{n+1}$ is the jth estimate of the solution vector at the nth $+ 1$ time step and Δt is the time step size. $\mathbf{K}$ is a matrix containing contributions from the non-linear advective and diffusive matrices $\mathbf{A}$ and $\mathbf{D}$, as well as from the mass and pressure matrices $\mathbf{M}$ and $\mathbf{C}$. It may be expressed as (ignoring subscripts for now)

$$\mathbf{K} = \frac{\mathbf{M}}{\Delta t} + \mathbf{A}(\mathbf{U}) + \mathbf{D}(\mathbf{U}) + \mathbf{C}. \tag{22}$$

Equation (21) is non-linear, and may be solved iteratively using the Newton–Raphson method. For this purpose, Equation (21) is rewritten in residual form:

$$\mathbf{R}_j(\boldsymbol{\Psi}_j^{n+1}, \boldsymbol{\Psi}^n, \Delta t) = \mathbf{K}(\boldsymbol{\Psi}_j^{n+1}, \Delta t)\boldsymbol{\Psi}_j^{n+1} - \mathbf{F}(\boldsymbol{\Psi}^n, \Delta t) = 0, \tag{23}$$

where subscripts denote the iteration number and superscripts the time step number. A truncated Taylor series expansion for $\mathbf{R}_j$ about $\boldsymbol{\Psi}_j^{n+1}$ gives

$$\mathbf{R}_j = \mathbf{R}_{j-1} + \frac{\partial \mathbf{R}_{j-1}}{\partial \boldsymbol{\Psi}_j^{n+1}} \Delta \boldsymbol{\Psi}_j = 0, \tag{24}$$

which gives

$$-\left[\frac{\partial \mathbf{R}_{j-1}}{\partial \boldsymbol{\Psi}_j^{n+1}}\right]^{-1} \Delta \boldsymbol{\Psi}_j = \mathbf{R}_{j-1}. \tag{25}$$

After solving Equation (25) for $\Delta \boldsymbol{\Psi}_j$, an update for $\boldsymbol{\Psi}_j^{n+1}$ is obtained from

$$\mathbf{\Psi}_j^{n+1} = \mathbf{\Psi}_{j-1}^{n+1} + \Delta\mathbf{\Psi}_j.$$

Convergence is declared when $\|\mathbf{R}_j\| < \epsilon_{\mathbf{R}}$, and $\|\Delta\mathbf{\Psi}_j\| < \epsilon_{\mathbf{\Psi}}$.

3. ANALYTICAL SENSITIVITY FORMULATION

Once the solution is computed, the outcome, as measured by a quantifiable scalar objective $G(\mathbf{\Psi}, \mathbf{b})$ may be evaluated. G generally depends on the solution $\mathbf{\Psi}$ and on various design parameters $\mathbf{b} \in \Re^n$, and is assumed to be continuous in design space. The optimization problem requires the minimization (or maximization) of G, subject to certain constraints, which may be written in a general form as $F_i(\mathbf{\Psi}, \mathbf{b}) = 0$. Gradient-type methods are available to efficiently traverse the design space to minimize (or maximize) G [37]. The design sensitivity, i.e. the gradient of G with respect to $\mathbf{b}$, may be computed by application of the chain rule:

$$\frac{\mathrm{d}G}{\mathrm{d}b_m} = \frac{\partial G}{\partial \mathbf{\Psi}} \frac{\mathrm{d}\mathbf{\Psi}}{\mathrm{d}b_m} + \frac{\partial G}{\partial b_m}, \tag{26}$$

where b_m is the mth component design parameter belonging to the design vector $\mathbf{b}$. Since G is an explicit function of $\mathbf{\Psi}$ and $\mathbf{b}$, $\partial G/\partial \mathbf{\Psi}$ and $\partial G/\partial b_m$ can be evaluated directly. However, the challenge in computing $\mathrm{d}G/\mathrm{d}b_m$ analytically lies in computing the response sensitivities $\mathrm{d}\mathbf{\Psi}/\mathrm{d}b_m$. This latter term describes how the solution vector ($\mathbf{U}_i$ and $\mathbf{P}$) varies with the design variables.

In this work, the direct differentiation method is used to compute the solution sensitivity $\mathrm{d}\mathbf{\Psi}/\mathrm{d}b_m$ [38]. The first step is to solve the forward problem for a base design. The preceding section detailed the formulation and solution of this non-linear problem. Once the solution is found, we have:

$$\mathbf{R}(\mathbf{\Psi}^{n+1}(\mathbf{b}), \mathbf{\Psi}^n(\mathbf{b}), \mathbf{b}) = 0. \tag{27}$$

Note that the design vector has been added to the residual definition to emphasize the implicit dependence of the solution on $\mathbf{b}$. Differentiation of Equation (27) with respect to b_m yields

$$\frac{\mathrm{d}\mathbf{R}}{\mathrm{d}b_m} = \frac{\partial \mathbf{R}}{\partial \mathbf{\Psi}^{n+1}} \frac{\mathrm{d}\mathbf{\Psi}^{n+1}}{\mathrm{d}b_m} + \frac{\partial \mathbf{R}}{\partial \mathbf{\Psi}^n} \frac{\mathrm{d}\mathbf{\Psi}^n}{\mathrm{d}b_m} + \frac{\partial \mathbf{R}}{\partial b_m} = 0. \tag{28}$$

Rearranging, we have

$$\left[\frac{\partial \mathbf{R}}{\partial \mathbf{\Psi}^{n+1}}\right] \frac{\mathrm{d}\mathbf{\Psi}^{n+1}}{\mathrm{d}b_m} = -\left[\frac{\partial \mathbf{R}}{\partial \mathbf{\Psi}^n} \frac{\mathrm{d}\mathbf{\Psi}^n}{\mathrm{d}b_m} + \frac{\partial \mathbf{R}}{\partial b_m}\right]. \tag{29}$$

Note that $\partial \mathbf{R}/\partial \mathbf{\Psi}^{n+1}$ is the same tangent stiffness used to obtain the forward solution (Equation (25)). The right-hand-side is called the pseudo-load vector. Thus, if a scheme such as LU decomposition is used to solve the linearized forward problem given by Equation (25), the sensitivity of the solution to the design variables, $\mathrm{d}\mathbf{\Psi}^{n+1}/\mathrm{d}b_m$, is readily (and efficiently) computed by back-substitutions of the pseudo-load terms $[(\partial \mathbf{R}/\partial \mathbf{\Psi}^{n+1})(\mathrm{d}\mathbf{\Psi}^n/\mathrm{d}b_m) + \partial \mathbf{R}/\partial b_m]$ into the previously decomposed tangent stiffness matrix from the forward solution. The reader is referred to previous works for further details [24,27,38]. Note that even if iterative linear solvers, such as preconditioned conjugate-gradient methods are used to solve the forward problem, the same preconditioner can be used to solve for the sensitivities.

3.1. Pseudo-loads for filling problems

The pseudo-load in Equation (29) consists of two quantities. The term $(\partial \mathbf{R}/\partial \mathbf{\Psi}^n)(\mathrm{d}\mathbf{\Psi}^n/\mathrm{d}b_m)$ contains the dependence of the response sensitivity at the current time step on those determined at previous time steps. Evaluation of this term is straightforward. The following sections outline the derivation of terms which go into forming the second quantity $\partial \mathbf{R}/\partial b_m$ for free-surface, turbulent filling problems. These form the bulk of this work.

The residual $\mathbf{R}$ is derived only from the Navier–Stokes equations and not from the filling equation, because the latter is linear and uncoupled from the Navier–Stokes equations (see Equation (7)), and it is solved explicitly. Thus, the methodology described in the preceding section refers to computation of the velocity and pressure sensitivities only. The relationship between the filling sensitivity and the velocity sensitivity is somewhat more complex, and it is described in Section 3.1.3.

To determine which quantities are needed to compute the pseudo-load, Equation (23) is differentiated with respect to a design variable:

$$\frac{\partial \mathbf{R}}{\partial b_m} = \frac{\partial \mathbf{K}}{\partial b_m}\,\mathbf{\Psi}^{n+1} - \frac{\partial \mathbf{F}}{\partial b_m}. \tag{30}$$

For the sake of brevity, the discussion is limited to the contribution of the diffusive term $\mathbf{D}$ to $\mathbf{K}$ (see Equations (17) and (22)), and the evaluation of $\partial \mathbf{D}/\partial b_m$. The results for the remaining terms are given in detail for non-filling problems in the work by Wang *et al.* [24].

The domain may itself depend on the design variables; therefore, the reference volume V_o is introduced and the integral is transformed to the reference domain:

$$D_{ij} = \int_{V_o} \mu J_{jn}^{-1}\,\frac{\partial \boldsymbol{\phi}}{\partial \xi_n}\,\frac{\partial \boldsymbol{\phi}^T}{\partial \xi_p}\,J_{ip}^{-T}\,|\mathbf{J}|\,\mathrm{d}V_o, \tag{31}$$

where V is the element volume in physical space, V_o is the volume in reference space and J_{jn} is the Jacobian of the transformation from the physical (j) to the reference (n) space. $\boldsymbol{\phi}$ denotes the finite element basis functions, and ξ_n denotes the isoparametric co-ordinates. Taking the partial derivative of D_{ij} with respect to b_m yields

$$\begin{aligned}\frac{\partial D_{ij}}{\partial b_m} = &\int_{V_o}\left(\frac{\partial \mu}{\partial b_m}\,J_{jn}^{-1}\,\frac{\partial \boldsymbol{\phi}}{\partial \xi_n}\,\frac{\partial \boldsymbol{\phi}^T}{\partial \xi_p}\,J_{ip}^{-T}\,|\mathbf{J}|\right)\mathrm{d}V_o\\ &+\int_{V_o}\mu\left(\frac{\partial J_{jn}^{-1}}{\partial b_m}\,\frac{\partial \boldsymbol{\phi}}{\partial \xi_n}\,\frac{\partial \boldsymbol{\phi}^T}{\partial \xi_p}\,J_{ip}^{-T} + J_{jn}^{-1}\,\frac{\partial \boldsymbol{\phi}}{\partial \xi_n}\,\frac{\partial \boldsymbol{\phi}^T}{\partial \xi_p}\,\frac{\partial J_{ip}^{-T}}{\partial b_m}\right)|\mathbf{J}|\,\mathrm{d}V_o\\ &+\int_{V_o}\mu J_{jn}^{-1}\,\frac{\partial \boldsymbol{\phi}}{\partial \xi_n}\,\frac{\partial \boldsymbol{\phi}^T}{\partial \xi_p}\,J_{ip}^{-T}\,\frac{\partial |\mathbf{J}|}{\partial b_m}\,\mathrm{d}V_o.\end{aligned} \tag{32}$$

The new terms required to evaluate this expression are $\partial \mu/\partial b_m$ and derivatives related to the Jacobian.

3.1.1. Design derivative of viscosity. The viscosity is defined as the sum of the molecular viscosity and a turbulent component $\mu = \mu_o + \mu_t$, so that from Equation (3) we have

$$\frac{\partial \mu}{\partial b_m} = \frac{\partial \mu_t}{\partial b_m} = \rho\left(2 l_t\,\frac{\partial l_t}{\partial b_m}\,S + l_t^2\,\frac{\partial S}{\partial b_m}\right). \tag{33}$$

To evaluate this expression, we must look more closely at the mixing length. The mixing length sensitivity was derived by Wang [24] and is based on Nikuradse's formula for pipe flows [30]. Here, a general form of the mixing length is used, which is based on empirical results for

boundary-layer channel flows [30,31]. In the finite element implementation of this model the mixing length is computed on an element-by-element basis. First, the distance of each element from a designated wall is computed, and then the appropriate mixing length for fluid in that location is computed according to the model shown in according to Figure 2. Specifically,

$$l_t = \min[\kappa l_i, \lambda\delta], \tag{34}$$

where l_i is the distance between the centroid of element i and the nearest wall. κ and λ are fixed, however, the value of δ is specified in advance for major regions in the flow path. In the runners, for example, δ is half the local runner width, in the mold cavity, δ is half the cavity width, etc. Therefore, if $l_t = \lambda\delta$, then $\partial l_t/\partial b_m = 0$. On the other hand, if $l_t = \kappa l_i$, then the mixing length sensitivity is an algebraic function of the nodal locations, the domain parameterization and the design velocity field [39–41]. The design velocity is defined as $\mathrm{d}x/\mathrm{d}b$, the derivative of nodal co-ordinates with respect to design variables. Thus, the mixing length sensitivity is non-zero only for those design variables which describe shape.

In addition to the mixing length sensitivity, $\partial\mu_t/\partial b_m$ also depends on $\partial S/\partial b_m$. The magnitude of the strain rate tensor is given by Equation (4). To compute the sensitivity of the magnitude of the strain rate tensor, the sensitivity of each component of the tensor must be computed. For this purpose, we write

$$\gamma_{ij} = \frac{\partial u_i}{\partial x_j} + \frac{\partial u_j}{\partial x_i} = \sum_n \left(\frac{\partial \phi_n}{\partial x_j} U_{in} + \frac{\partial \phi_n}{\partial x_i} U_{jn} \right) = \sum_n \left(J^{-1}_{jk} \frac{\partial \phi_n}{\partial \xi_k} U_{in} + J^{-1}_{ik} \frac{\partial \phi_n}{\partial \xi_k} U_{jn} \right). \tag{35}$$

Then, differentiating γ_{ij} with respect to b_m,

$$\frac{\partial \gamma_{ij}}{\partial b_m} = \sum_n \left[\frac{\partial (J^{-1}_{jk})}{\partial b_m} \frac{\partial \phi_n}{\partial \xi_k} U_{in} + \frac{\partial (J^{-1}_{ik})}{\partial b_m} \frac{\partial \phi_n}{\partial \xi_k} U_{jn} \right]. \tag{36}$$

Once again, we find derivatives of the Jacobian. Expressions for the design derivative of the Jacobian have been derived previously for fixed domains [24], but further work is required to consider filling problems.

3.1.2. Design derivative of Jacobian for filling problems. The filling fraction f_i affects the flow equations by modifying the domain over which the flow equations are solved. For partially filled elements, the finite element quantities are computed by performing the integrations over a reduced element volume. The ratio of the volume of this reduced element V_r to the parent element V_i is the filling fraction for that element (see Figure 3).

As an example, consider again the formation of the diffusive finite element matrix, D_{ij} (Equation (31)). In this equation J accounts only for the difference in shape and size of the element in the physical space to that in the reference domain. However, for a partially filled element this Jacobian must also account for the reduced size of the element in real space. In Figure 3, ${}_{\mathrm{f}}J$ and ${}_{\mathrm{pf}}J$ represent the transformations for full and partially full elements respectively. The difference between these terms depends on the filling fraction for that element, f_i

Thus, in a filling problem, $\partial J/\partial b_m$ in Equation (32) is replaced by $\partial({}_{\mathrm{pf}}J)/\partial b_m$. The first contribution to $\partial({}_{\mathrm{pf}}J)/\partial b_m$ comes from the domain parameterization representing the sensitivity due to external changes in the shape of the domain, and is accounted for in the previous work [24]. The second contribution arises from the sensitivity of the filling front position to any design variable, not just shape. The design derivatives of ${}_{\mathrm{pf}}J^{-T}$ and $\left|{}_{\mathrm{pf}}J\right|$ are both based on the term $\partial({}_{\mathrm{pf}}J)/\partial b_m$, so the evaluation of the latter will be the focus of discussion.

Consider the Jacobian of transformation from the physical j-frame to the reference k-frame for a partially filled element at a single integration point, denoted by l:

$$ {}_{\mathrm{pf}}J_{jkl} = \sum_{n}^{n\mathrm{nod}} \left(\frac{\partial \phi_{nl}}{\partial \xi_k} \right) {}_{\mathrm{r}}x_{jn}, \tag{37} $$

where $\partial({}_{\mathrm{r}}x_{jn})/\partial b_m$ is the vector of the j-direction co-ordinates of node n of the reduced element in physical space. $\partial \phi_{nl}/\partial \xi_k$ is the derivative of the shape function associated with node n, with respect to the isoparametric co-ordinate ξ_k at Gauss point l.

Taking the derivative with respect to a design variable:

$$ \frac{\partial({}_{\mathrm{pf}}J_{jkl})}{\partial b_m} = \sum_{n}^{n\mathrm{nod}} \left(\frac{\partial \phi_{nl}}{\partial \xi_k} \right) \frac{\partial({}_{\mathrm{r}}x_{jn})}{\partial b_m}, \tag{38} $$

where ${}_{\mathrm{r}}x_{jn}$ consists of the two contributions mentioned previously. This term represents how the nodes of the element change as a function of design and of the element filling fraction (see Figure 3). The nodal co-ordinates of this reduced element are evaluated from

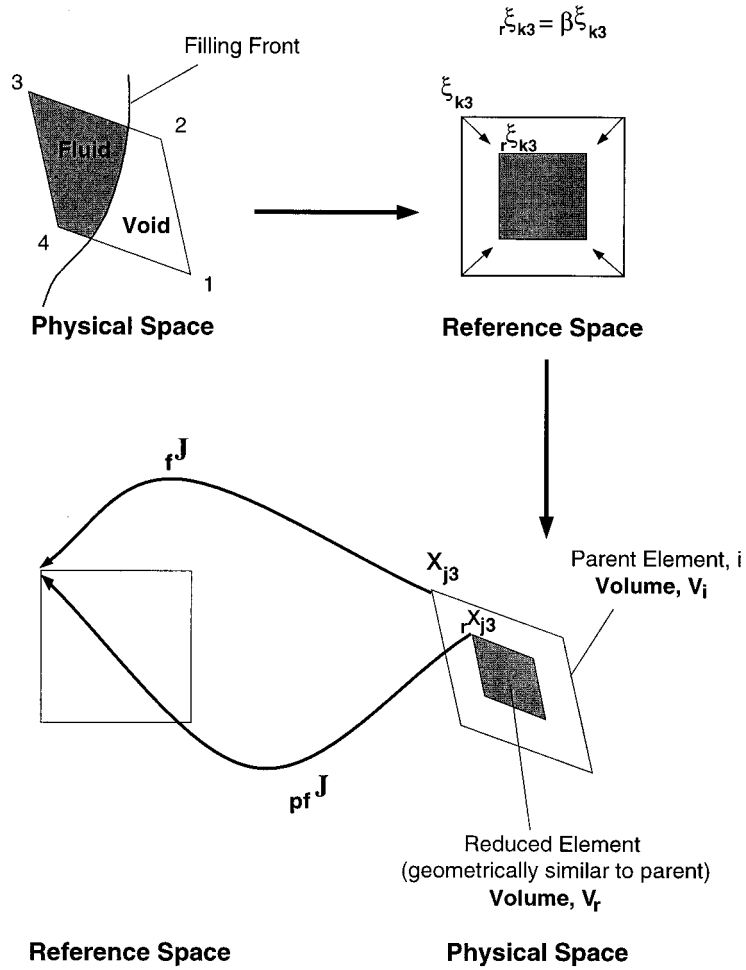

Figure 3. Integration domain and transformation for partially full elements.

$$ {}_{\mathrm{r}}x_{jn} = \sum_{n}^{n\mathrm{nod}} \phi_n({}_{\mathrm{r}}\xi_{kn}) x_{jn}, \tag{39} $$

where $x_{jn}/\partial b_m$ are the global co-ordinates of the n-nodes of the parent element in the j-direction. ${}_{\mathrm{r}}\xi_{kn}$ are the k-direction isoparametric co-ordinates of node n of the reduced element, defined as

$$ {}_{\mathrm{r}}\xi_{kn} = \beta \xi_{kn}. \tag{40} $$

β is related to the filling fraction by

$$ \beta = \begin{cases} \sqrt{f_i}: & 2-D \\ \sqrt[3]{f_i}: & 3-D \end{cases}. \tag{41} $$

This formulation has the effect of forming a reduced element which is geometrically similar to the parent element (see Figure 3). The total sensitivity of the nodal co-ordinate to design is obtained by differentiating Equation (39) with respect to b_m:

$$ \frac{\partial({}_{\mathrm{r}}x_{jn})}{\partial b_m} = \sum_{n}^{n\mathrm{nod}} \left(\frac{\partial \phi_n({}_{r}\xi_{kn})}{\partial b_m} x_{jn} + \phi_n({}_{\mathrm{r}}\xi_{kn}) \frac{\partial(x_{jn})}{\partial b_m} \right), \tag{42} $$

where $\Sigma_n^{n\mathrm{nod}} \phi_n({}_{\mathrm{r}}\xi_{jn})(\partial x_{jn}/\partial b_m)$ is the contribution due to the domain parameterization. In addition, the term $\partial \phi_n/\partial b_m$ is non-zero, because $\phi_n({}_{\mathrm{r}}\xi_{kn})$ is evaluated at the *reduced* local co-ordinates of the element, and is therefore a function of the design variables, through the filling fraction. Thus, in general, the shape functions may be expressed as $\phi_n(\beta(\mathbf{b}), \xi_{kn})$, in which case, the term $\partial \phi_n/\partial b_m$ can be evaluated as

$$ \frac{\partial \phi_n({}_{\mathrm{r}}\xi_{kn})}{\partial b_m} = \frac{\partial \phi_n}{\partial \beta} \frac{\partial \beta}{\partial b_m}. \tag{43} $$

This discussion can be clarified by introducing an example. Consider a nine-noded quadratic element and select the shape function associated with node 1 (ϕ_1) at $(\xi_{11}, \xi_{21}) = (1, -1)$, then evaluate it at the point given by ${}_{\mathrm{r}}\xi_{11} = \beta \xi_{11}$, ${}_{\mathrm{r}}\xi_{21} = \beta \xi_{21}$. The shape function is given by

$$ \phi_1 = \frac{1}{4} \beta^2 \xi_{11} \xi_{21} (1 - \beta \xi_{11})(1 - \beta \xi_{21}). \tag{44} $$

$\partial \phi_1/\partial \beta$ may be evaluated by differentiating Equation (44):

$$ \frac{\partial \phi_1}{\partial \beta} = \frac{1}{4} \beta \xi_{11} \xi_{21} \{ -\beta[(1 - \beta \xi_{11})\xi_{21} + (1 - \beta \xi_{21})\xi_{11}] + 2(1 - \beta \xi_{11})(1 - \beta \xi_{21}) \} \tag{45} $$

$$ = \frac{1}{2} \beta \{1 - 2\beta^2\}, \tag{46} $$

and $\partial \beta/\partial b_m$ is given by

$$ \frac{\partial \beta}{\partial b_m} = \frac{1}{2\sqrt{f_i}} \frac{\partial f_i}{\partial b_m}. \tag{47} $$

Therefore, it is clear that the filling fraction sensitivity will affect the velocity sensitivity, even though the filling fraction does not appear explicitly in the Navier–Stokes equations. The filling fraction, and thus its sensitivity $\mathrm{d}f_i/\mathrm{d}b_m$, are computed before the velocity sensitivity, so $\partial \beta/\partial b_m$ and thus $\mathrm{d}J^{-T}/\mathrm{d}b_m$, etc. can be evaluated readily. The following section describes the computation of the filling fraction sensitivity.

3.1.3. VOF sensitivity. To compute the filling fraction sensitivity, we begin by differentiating Equation (7) with respect to the design variables b_m:

$$\frac{\mathrm{d}f_i^{n+1}}{\mathrm{d}b_m} = \frac{\mathrm{d}f_i^n}{\mathrm{d}b_m} + \frac{\Delta t}{V_i^2}\left[V_i \sum_k \frac{\mathrm{d}Q_{ik}^n}{\mathrm{d}b_m} - \sum_k Q_{ik}^n \frac{\mathrm{d}V_i}{\mathrm{d}b_m}\right] + \left[\frac{1}{V_i}\sum_k Q_{ik}^n\right]\frac{\mathrm{d}(\Delta t)}{\mathrm{d}b_m}. \tag{48}$$

It is clear from Equation (48) that the sensitivities of several quantities must be computed. These include the flow rate sensitivity $\mathrm{d}Q_{ik}^n/\mathrm{d}b_m$, the element volume sensitivity $\mathrm{d}V_i/\mathrm{d}b_m$, and the sensitivity of the filling time step, $\mathrm{d}(\Delta t)/\mathrm{d}b_m$.

The flux Q_{ik}^n is composed of two parts, an integrated flux and a contact area factor, as shown in Equation (8). Thus, the flux sensitivity can be expressed as

$$\frac{\mathrm{d}Q_{ik}^n}{\mathrm{d}b_m} = -\alpha_{ik}\left[\int_{\Omega_k}\left\{\frac{\mathrm{d}\mathbf{u}^n}{\mathrm{d}b_m}\cdot\hat{\mathbf{n}} + \mathbf{u}^n\cdot\frac{\mathrm{d}\hat{\mathbf{n}}}{\mathrm{d}b_m}\right\}\mathrm{d}\Omega_k\right] - \frac{\mathrm{d}\alpha_{ik}}{\mathrm{d}b_m}\int_{\Omega_k}\mathbf{u}^n\cdot\hat{n}\,\mathrm{d}\Omega_k. \tag{49}$$

The term $\mathrm{d}\mathbf{u}^n/\mathrm{d}b_m$ is the velocity sensitivity from the previous time step, because the filling fraction sensitivity is computed before the velocity sensitivity and is therefore known. The effect of the filling fraction sensitivity on the velocity sensitivity was discussed in Section 3.1.2.

$\mathrm{d}\hat{\mathbf{n}}/\mathrm{d}b_m$ is the sensitivity of the unit normal direction for element side k. This term is zero, unless the design variable defines the shape, in which case $\mathrm{d}\hat{\mathbf{n}}/\mathrm{d}b_m$ is readily computed from the domain parameterization and element description [40].

Finally, $\mathrm{d}\alpha_{ik}/\mathrm{d}b_m$ relates the flow front shape to the design. The filling front position is reconstructed from the filling fraction of partially filled elements and their neighbors. As previously indicated, there are several possible configurations that are considered to reconstruct the interface. Using the filling fraction sensitivities from the previous time step, $\mathrm{d}\alpha_{ik}/\mathrm{d}b_m$ can be computed readily through algebraic combinations of these sensitivities.

The volume (i.e. the area in 2D) of element i, V_i, is computed algebraically:

$$V_i = 0.25(ch - df), \tag{50}$$

where

$$c = x_{12} + x_{13} - (x_{11} + x_{14}), \qquad d = x_{22} + x_{23} - (x_{21} + x_{24}), \qquad f = x_{13} + x_{14} - (x_{11} + x_{12}),$$

$$h = x_{23} + x_{24} - (x_{21} + x_{22}).$$

As before, x_{jn} are the j-direction co-ordinates of node n of the element. This equation also holds for straight-sided nine-noded quadrilaterals used in this work. Thus, the sensitivity expression is straightforward:

$$\frac{\mathrm{d}V_i}{\mathrm{d}b_m} = 0.25\left[c\frac{\mathrm{d}h}{\mathrm{d}b_m} + h\frac{\mathrm{d}c}{\mathrm{d}b_m} - d\frac{\mathrm{d}f}{\mathrm{d}b_m} - f\frac{\mathrm{d}d}{\mathrm{d}b_m}\right], \tag{51}$$

where

$$\frac{\mathrm{d}c}{\mathrm{d}b_m} = \frac{\mathrm{d}x_{12}}{\mathrm{d}b_m} + \frac{\mathrm{d}x_{13}}{\mathrm{d}b_m} - \left(\frac{\mathrm{d}x_{11}}{\mathrm{d}b_m} + \frac{\mathrm{d}x_{14}}{\mathrm{d}b_m}\right), \tag{52}$$

$$\frac{\mathrm{d}d}{\mathrm{d}b_m} = \frac{\mathrm{d}x_{22}}{\mathrm{d}b_m} + \frac{\mathrm{d}x_{23}}{\mathrm{d}b_m} - \left(\frac{\mathrm{d}x_{21}}{\mathrm{d}b_m} + \frac{\mathrm{d}x_{24}}{\mathrm{d}b_m}\right), \tag{53}$$

$$\frac{\mathrm{d}f}{\mathrm{d}b_m} = \frac{\mathrm{d}x_{13}}{\mathrm{d}b_m} + \frac{\mathrm{d}x_{14}}{\mathrm{d}b_m} - \left(\frac{\mathrm{d}x_{11}}{\mathrm{d}b_m} + \frac{\mathrm{d}x_{12}}{\mathrm{d}b_m}\right), \tag{54}$$

$$\frac{\mathrm{d}h}{\mathrm{d}b_m} = \frac{\mathrm{d}x_{23}}{\mathrm{d}b_m} + \frac{\mathrm{d}x_{24}}{\mathrm{d}b_m} - \left(\frac{\mathrm{d}x_{21}}{\mathrm{d}b_m} + \frac{\mathrm{d}x_{22}}{\mathrm{d}b_m} \right). \tag{55}$$

$\mathrm{d}x_{jn}/\mathrm{d}b_m$ are the sensitivities of the j-direction co-ordinates of node j to design variable m, as given by the domain parameterization. Similar expressions may be derived for 2D axisymmetric and 3D elements.

Finally, the time step for integration of the VOF equation is computed from Equation (9). The sensitivity of the time step is forced to be zero by specifying the time step sizes *a priori*. This is accomplished by running the algorithm on the base design with no subcycling, and recording the time steps used. These recorded time steps are the minimum of Δt_{fill} and Δt_{flow} (see Equations (9) and (10)) for which the non-linear iteration converged. These time steps are then used for all subsequent gradient and function evaluations, and are thus independent of design.

4. EXAMPLE APPLICATION

An example casting is created to illustrate a design optimization method based on the sensitivity computations described in the previous chapters. A thick block casting is fed from two runners through four ingates. The design is symmetric, and the runners and gates are sized according to the published design rules [1]. Physical experiments have also been performed to evaluate the applicability of the mixing length model to casting-mold filling flows, and to evaluate the success of the optimal design. The results of these experiments are presented in a separate publication [42].

4.1. Sensitivity verification

Prior to performing the example optimization, the analytical sensitivities computed by the newly-developed algorithm are checked by comparison with finite difference approximations. The discrepancy between the analytical and finite-difference sensitivities is an order of 10^{-4}% of the sensitivity value, as illustrated in Figure 4 for a typical test problem. Table I shows the computational advantage of evaluating the sensitivities analytically.

The data in the table suggests the approximate sensitivity cost formula: $C_m = (\eta + \zeta m) * t_{\mathrm{Base}}$, where C_m is the additional cost of evaluating m sensitivities, and t_{Base} is the base simulation time. η and ζ are constants. Therefore, η and ζ may be evaluated for this problem, giving

$$C_m = [0.1 + 0.14m] * t_{\mathrm{Base}}. \tag{56}$$

Whereas, for a finite difference calculation, $C_m = m * t_{\mathrm{Base}}$.

4.2. Geometry, mesh and boundary conditions

Figure 5 shows the geometry and mesh used as the base design in this example. The choke area at the sprue base, upon which the other areas are based, is computed to give an AFS-recommended pouring rate of 4 lb s^{-1} (8.8 kg s^{-1}) for aluminum. The recommended sprue:runner:ingate area ratio is 1:4:4. Assuming uniform thickness in the z-direction, the sprue, runner and gate widths (in 2D) are 24.1, 48.5 and 24.2 mm, respectively. The runner cross-section is reduced after the first ingate to promote uniform filling through all the ingates. Additionally, the ingate further from the sprue is 5% larger than the one closer to the sprue, to compensate for frictional loss. Finally, the radius of the bend in the runner is 25.4 mm. These dimensions and adjustments are all consistent with the existing design rules [1].

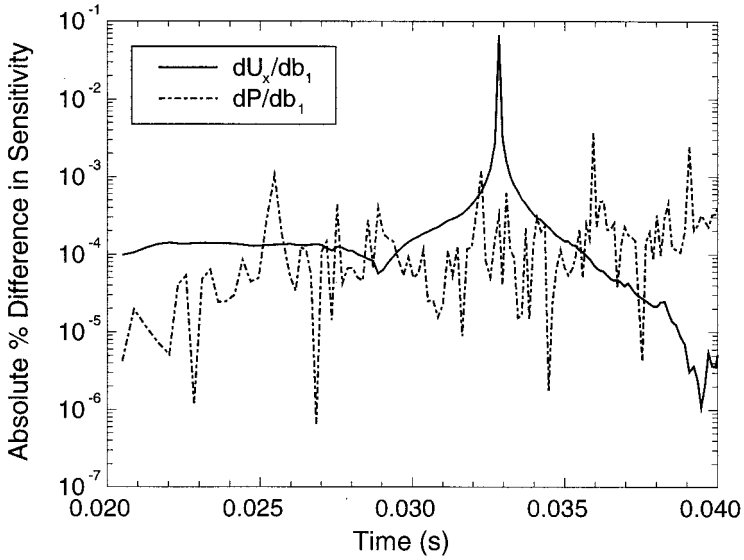

Figure 4. Percentage difference between analytical and finite difference shape sensitivities.

The finite element mesh consists of 314 nine-noded quadrilateral elements and 1414 nodes. Quadratic elements are specifically chosen to enhance the performance of the algorithm, because large elements permit larger time steps (see Equation (9)). This element type permits the use of a nodal density sufficient to resolve the boundary layer, but with larger elements.

The sprue itself is not modeled. Instead, a pressure boundary condition is applied at the inlet of the model, which corresponds to the sprue base. The prescribed pressure of 9.13 MPa is equivalent to a 355 mm head of aluminum. The no-slip boundary condition is applied to all walls except the center line, where a symmetry boundary condition is applied ($\partial u_y/\partial x = 0$ and $u_x = 0$). Finally, gravity acts in the direction shown in Figure 5.

4.3. Base solution

The filling pattern for the base design shown in Figure 6 was first determined. This pattern indicates that mold gas aspiration will potentially occur in two locations in the runner system (labeled regions A and B and shaded in Figure 6). The shaded regions are bounded by the runner walls and the fluid front, given by the 0.5 filling-fraction contour. In these regions, the fluid momentum is so high that the stream cannot conform to the shape of the runner as it bends. As a result, pockets of low-pressure liquid (eddies) or air may form at these locations,

Table I. Comparison of analytical and finite-difference sensitivities

No. design variables	Time in CPU (s)			
	Base	Analytical sensitivities	Finite-difference sensitivities	Time savings (%)
2	20 375	27 225	61 125	125
9	20 375	40 988	203 750	397

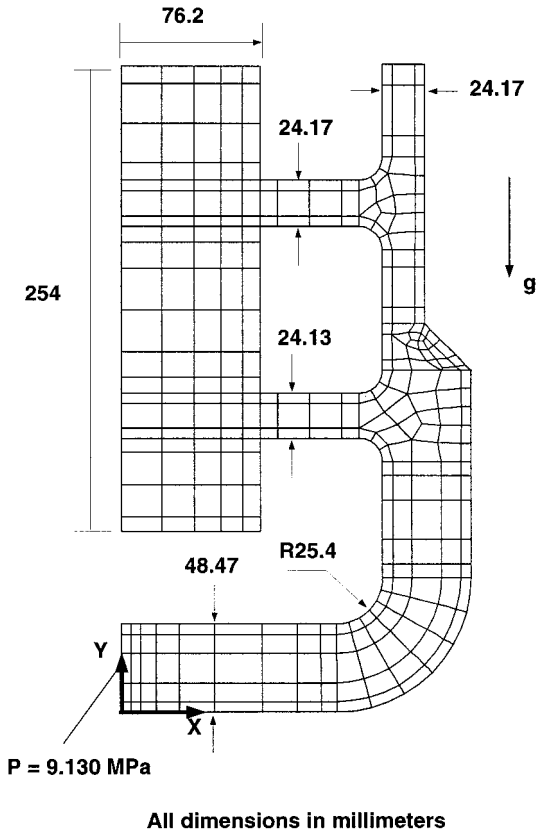

Figure 5. 2D finite element mesh showing the base design.

and mold gases may be aspirated into the metal. Therefore, to reduce the possibility of mold-gas aspiration and churning of the liquid stream, the runners will be designed so that these pockets do not form.

4.4. Optimization formulation

4.4.1. Objective. The design objective is to eliminate the low pressure regions in the runner system. This can be accomplished by maximizing the amount of fluid in contact with the walls of the runners in the target locations A and B. This will force the runners to conform to the desired shape of the fluid stream, thereby discouraging flow separation in regions A and B. To achieve this, an objective function G is defined, to be maximized, where

$$G = \sum_{i}^{N_A} f_i + \sum_{j}^{N_B} f_j, \tag{57}$$

where f_i is the ith element filling fraction, N_A and N_B are the number of elements in regions A and B respectively.

4.4.2. Design variables. Eight design variables are chosen to parameterize the shape of the runners. To facilitate an automated optimization scheme, the domain is parameterized so that a single design variable describes the movement of all nodal co-ordinates in the mesh change

in response to changes in that variable. Thus, the part shape and mesh can be modified simply by changing the design variables, using

$$x_j = x_j^o + \sum_m \frac{\mathrm{d}x_j}{\mathrm{d}b_m} \Delta b_m, \tag{58}$$

following the natural design method developed by Choi et al. [39] and Tortorelli et al. [40]. x_j are the new j-direction co-ordinates of any node in the mesh, and x_j^o are their initial values. Such a domain parameterization permits the quantity $\Sigma_n^{n\mathrm{mod}} \phi_n({}_{\mathrm{r}}\xi_{kn})(\partial x_{jn}/\partial b_m)$ in Equation (42) to be defined *a priori*. Figures 7 and 8 show the runner shape changes and corresponding mesh deformations for the eight design variables for $\Delta b_i = 10$. To highlight the domain parameterization, the outline of the undeformed shape is superimposed on the deformed mesh, and the region of interest is shaded.

4.5. Optimization algorithm

The optimization methodology is summarized in Figure 9. It is completely automated, once the domain parameterization and objective definition are complete. The analytical sensitivities of the fluid front position, given by the element filling fractions, is computed by the modified version of FIDAP™. From these solution sensitivities, the objective sensitivities are evaluated and passed to DOT [43], a commercially available optimization code, along with the value of the objective. The numerical optimizer systematically modifies the design variables to maximize the objective. The BFGS algorithm was chosen because the only constraints in the optimization problem are 'side constraints', i.e. limits on the maxima and minima for the components b_m.

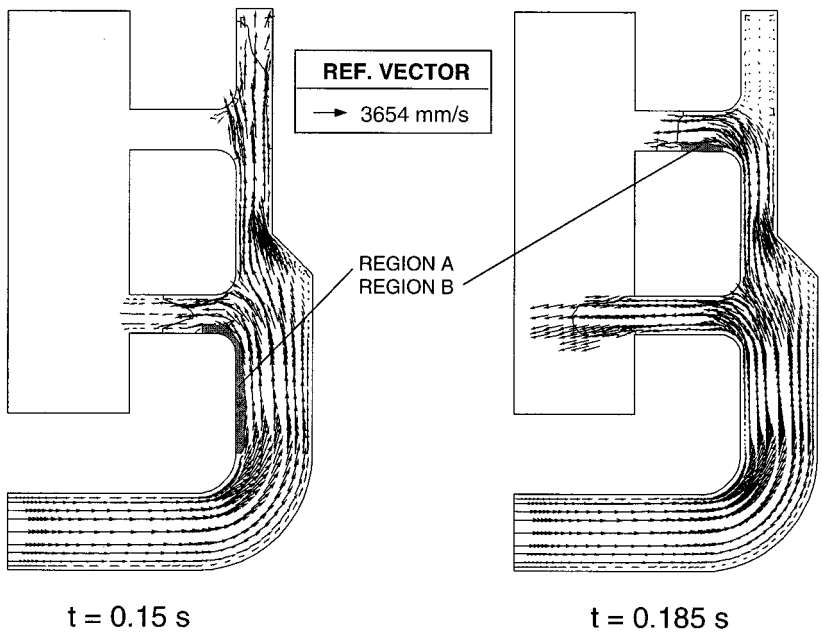

Figure 6. Base solution at $t = 0.15$ and 0.185 s showing target regions A and B.

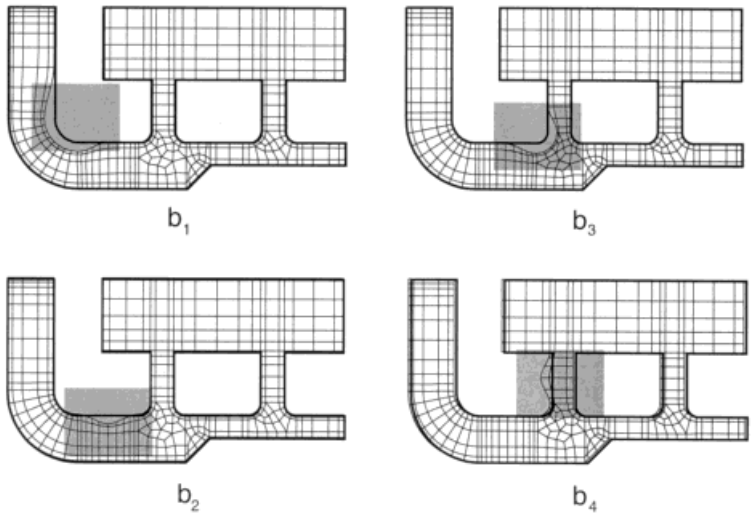

Figure 7. Mesh deformation for design variables b_1–b_4.

4.6. Optimization results

Figure 10 shows the history of the objective function for this optimization. The optimization is terminated when the objective between two consecutive iterations differs by $< 0.1\%$. The initial objective value is scaled to unity.

At termination, the objective was improved by 27%. This change in the objective corresponds to a change in the solution, as shown in Figure 11. As this figure shows, when viewed in comparison with the base solution in Figure 6, the optimization produces the desired effect of eliminating the pockets formed in runners. Figure 12 clearly shows the runner shapes of the optimal design compared with the outline of the original shape.

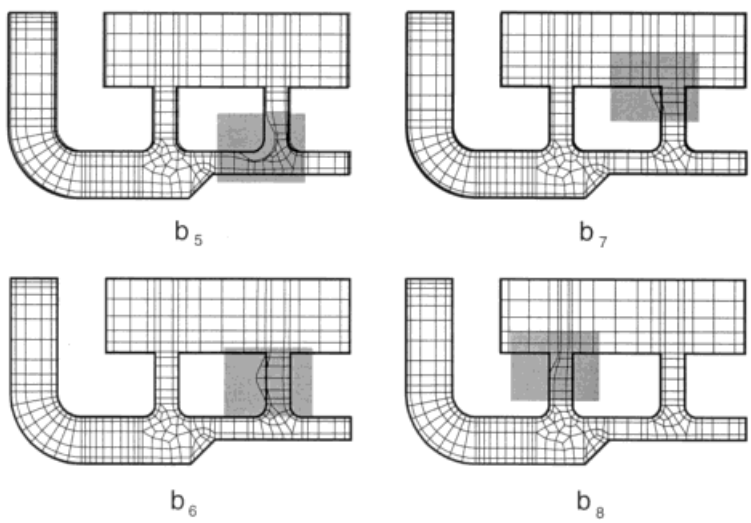

Figure 8. Mesh deformations for design variables b_5–b_8.

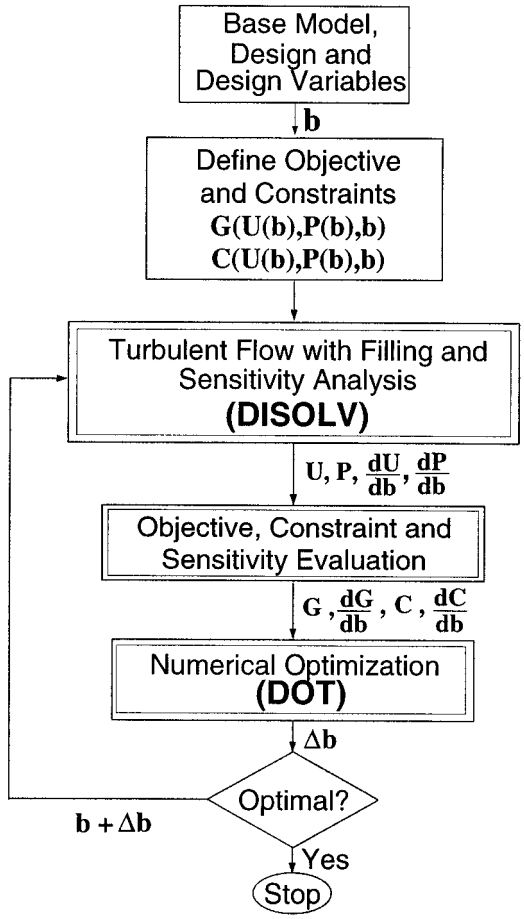

Figure 9. Schematic of optimization method.

The optimal runner shapes are reasonable in relation to the expected result. To minimize the likelihood of fluid separation in the runner system, the radius of curvature of the bends should be as large as possible. It is clear from the result that this configuration is achieved at two of the critical turns in the runner system.

5. CONCLUSION

The results of this work clearly show that a design optimization methodology, combining finite element analysis and analytical sensitivity computation, can be applied successfully for rigging design. Future work will focus on two areas. The first is to verify the suitability of the mixing length model for modeling turbulence in simple filling examples, by conducting physical tests. The second is to apply the method to more complex filling situations, for which the VOF method is particularly suited. Additionally, in future applications, other objectives and constraints will also be investigated. For example, maximizing the filling rate while avoiding mold erosion is possible. In this case the constraint will involve the shear stress at the runner wall.

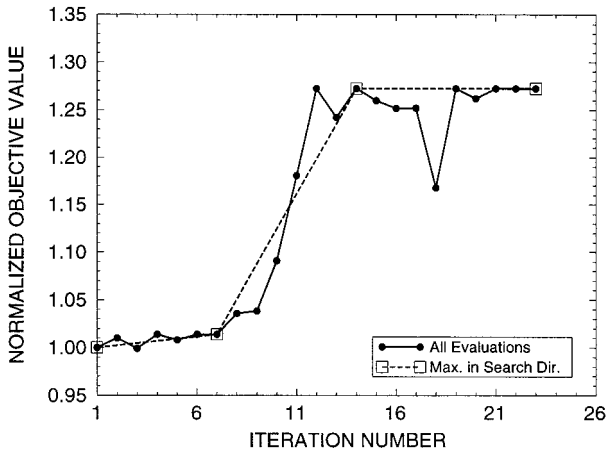

Figure 10. Optimization history.

An additional challenge is to improve the performance of the sensitivity algorithm. The speed of the algorithm is critical to the feasibility of performing 3D filling optimizations. Faster simulations are possible by allowing filling time steps to subcycle within flow time steps. In the current implementation, the overall time step is forced to be the minimum of the Courant time step (for filling) and the variable time step (for flow). To compute the flow field sensitivities in the subcycling case, the contribution of the variable time step sensitivity will have to be included.

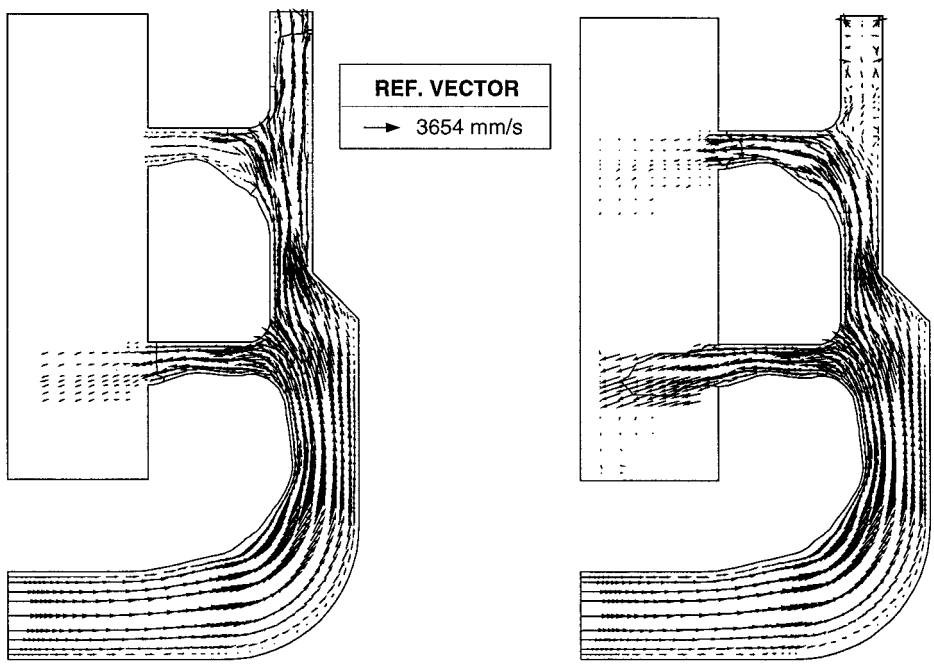

Figure 11. Optimal solutions at t = 0.15 and 0.185 s.

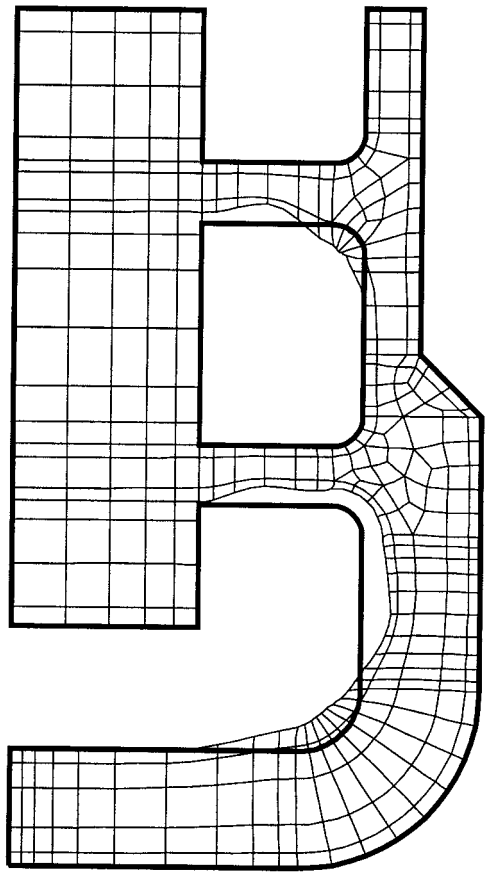

Figure 12. Deformed mesh representing optimal runner shapes.

Finally, because of the case-based nature of the VOF implementation in FIDAP™, the filling solution is not continuous in design space. This fact is particularly evident when checking the analytical sensitivities by a finite difference. For perturbations as small as 1.0E-6 in the design variables, different paths through the code are sometimes chosen. This is equivalent to a bifurcation in the design space for that value of the design variable, making comparisons of the finite difference values with the analytical values inaccurate. Therefore, although the gradients are evaluated correctly at a certain design, a step in the resulting search direction may actually have an unpredicted effect. However, this is also the case for irregular but continuous objective surfaces with many peaks and valleys. In these cases, as in the current work, more gradient evaluations will be necessary to traverse the design space successfully. This fact further underscores the need to compute the gradients in an efficient manner, such as that used in this work.

ACKNOWLEDGMENTS

This work was based on analytical sensitivity methods originally developed by Professor Daniel Tortorelli. We would also like to thank him for his input and contributions to this work. Additionally, the authors wish to thank and acknowledge Ford Motor Company for its

support under the University Research Program, and Ford Casting Research Grant. In particular, we thank Dr. Nagendra Palle, program liasion at Ford Scientific Research Lab, for helpful comments and suggestions.

APPENDIX A. NOMENCLATURE

Symbol	Description	Value
$\mathbf{A}(\mathbf{U}_i)$	finite element advection matrix	
$\mathbf{b}$	vector of design variables	
$\mathbf{C}$	gradient operator matrix	
$\mathbf{D}(\mathbf{U}_i)$	finite element diffusion matrix	
$\mathbf{F}$	finite element force vector	
$F_i(\mathbf{\Psi}, \mathbf{b})$	vector of constraints	
f_i	filling fraction for element i	
Fr	Froude number	U_c^2/gL
g	acceleration due to gravity, mm s^{-2}	9810
$\mathbf{g}$	bodyforce vector per unit volume	
$G(\mathbf{\Psi}, \mathbf{b})$	scalar objective function	
Gz	Graetz number	$U_c h/\alpha$
J	Jacobian of finite element transformation	Q
${}_{\mathrm{pf}}J$	Jacobian for a partially filled element	
${}_{\mathrm{f}}J$	Jacobian for a completely full element	
l_{t}	turbulent mixing length, mm	
$\mathbf{K}$	global finite element global stiffness matrix	
$\mathbf{M}$	finite element mass matrix	
$\hat{\mathbf{n}}$	unit normal to element side	
p	continuum pressure	
$\mathbf{P}$	global pressure solution vector	
q_{ik}	normalized flow rate across side k of element i, $\mathrm{mm}^2\ \mathrm{s}^{-1}$	
Q_{ik}	flow rate across side k of element i, $\mathrm{mm}^2\ \mathrm{s}^{-1}$	
$\mathbf{R}$	global finite element residual vector	
Re	Reynolds number	$\rho U_c L/\mu$
S	magnitude of strain rate tensor	$\dot{\boldsymbol{\gamma}}:\dot{\boldsymbol{\gamma}}$
t	time, s	
U_c	characteristic velocity, mm s^{-1}	
$\mathbf{u}$	continuum velocity vector	
$\mathbf{U}_i$	global nodal velocity solution vector in the i-direction	
V_i	volume of element i in real space, mm^3	
V_o	volume of element i in reference space, mm^3	
x_{jn}	global j-direction co-ordinate of node n in parent element	
${}_{\mathrm{r}}x_{jn}$	global j-direction co-ordinate of node n in reduced element	
We	Weber number	$\rho U_c L/\sigma'$
Greek letters		
α_{ik}	geometric factor which scales q_{ik}	function of f_i

α	thermal diffusivity, $mm^2\ s^{-1}$	$k/\rho c_p$
δ	mixing-length model-boundary layer depth, mm	
$\epsilon_{\mathbf{R}}$	residual convergence tolerance	10^{-6}
$\epsilon_{\mathbf{\Psi}}$	solution convergence-rate tolerance	10^{-6}
$\boldsymbol{\phi}$	velocity interpolation (shape) function	
Γ	Courant number	≈ 0.2
$\dot{\boldsymbol{\gamma}}$	strain rate tensor	
$\dot{\gamma}_{ij}$	*ij*-component of strain rate tensor	$(\partial u_i/\partial x_j)+(\partial u_j/\partial x_i)$
κ	Von Karman constant	0.41
λ	empirical mixing length constant	0.09
μ	viscosity, $gmm^{-1}\ s^{-1}$	1.4×10^{-3}
μ_o	molecular viscosity	
μ_t	turbulent eddy viscosity	
θ	VOF pseudo-concentration variable	
ρ	density, $g\ mm^{-3}$	2.7×10^{-3}
σ_i	surface tractions, $N\ mm^{-2}$	
σ^t	surface tension coefficient of liquid Al in air, $N\ mm^{-1}$	1.6
ξ_{kn}	*k*-direction isoparametric co-ordinate for node *n* in parent element	
${}_r\xi_{kn}$	*k*-direction isoparametric co-ordinate for node *n* in reduced element	
$\mathbf{\Psi}$	global solution vector	$\mathbf{\Psi}(\mathbf{U}_i, \mathbf{P})$
$\boldsymbol{\psi}$	pressure interpolation (shape) function	

REFERENCES

1. AFS, ed., *Basic Principles of Gating and Risering*, AFS Cast Metals Institute, 1973.
2. R. Heine, C. Loper and P. Rosenthal, *Principles of Metal Casting*, 2nd edn, McGraw-Hill, New York, 1967.
3. ASM, ed., *Casting Design Handbook*, Reinhold, New York, 1962.
4. C. Hirt and B. Nichols, 'Volume of fluid (VOF) method for the dynamics of free boundaries', *J. Comput. Phys.*, **39**, 201–225 (1981).
5. F. Mashayek and N. Ashgriz, 'A hybrid finite-element-volume-of-fluid method for simulating free surface flows and interfaces', *Int. J. Numer. Methods Fluids*, **20**, 1363–1380 (1995).
6. R. Lewis, A. Usmani and J. Cross, 'Efficient mould filling simulation in castings by and explicit finite element method', *Int. J. Numer. Methods Fluids*, **20**, 493–506 (1995).
7. Y.-F. Zhang, W. Liu and H.-P. Wang, 'Cast filling simulations of thin-walled cavities', *Comput. Methods Appl. Mech. Eng.*, **128**, 199–230 (1995).
8. M. Barkhudarov, H. You, J. Ortega, J. Beech, S. Chin and D. Kirkwood, 'Experimental validation and development of FLOW-3D for casting problems', *Model. Cast. Weld. Adv. Solidif. Proc.*, **VI**, 421–434 (1993).
9. J.-L. Yeh, S.-H. Jong, C.-W. Chen and W.-S. Hwang, 'An improved model for the filling of castings and its experimental verification', *Model. Cast. Weld. Adv. Solidif. Proc.*, **VI**, 451–458 (1993).
10. H. Ota, Y.S.M. Ninomiya and Y. Ueda, 'Correlation between the hot strength of an organic binder mould and mould erosion', *Foundryman*, **82**, 278–283 (1989).
11. F. Bradley and S. Heinemann, 'A hydraulics-based/optimization methodology for gating design', *Appl. Math. Model.*, **17**, 406–414 (1993).
12. Y. Park and K. Choi, 'Configuration design sensitivity analysis of nonlinear structural systems with elastic material', *Mech. Struct. Mach.*, **24**, 217–255 (1996).
13. A. Valido, L. Sousa and C. Barradas, 'Optimal cross-section and configuration design of cyclic loaded elastic-plastic structures', *Struct. Eng. Mech.*, **4**, 25–35 (1996).
14. Y. Tada and M.N.R. Matsumoto, 'Optimum structural design considering vibration control', *JSME Int. J.*, Series 3, **35**, 413–420 (1992).

15. S. Afonso and E. Hinton, 'Free vibration analysis and shape optimization of variable thickness plates and shells-ii. Sensitivity analysis and shape optimization', *Comput. Syst. Eng.*, **6**, 47–66 (1995).
16. R. Reitinger and E. Ramm, 'Buckling and imperfection sensitivity in the optimization of shell structures', *Thin-Walled Struct.*, **23**, 159–177 (1995).
17. R. Haftka, 'Techniques for thermal sensitivity analysis', *Int. J Numer. Methods Eng.*, **17**, 71–80 (1981).
18. R. Meric, 'Boundary integral equation and conjugate gradient methods for optimal boundary heating of solids', *Int. J. Heat Mass Trans*, **26**, 261–267 (1983).
19. R. Meric, 'Boundary element methods for optimization of distributed parameter systems', *Int. J. Numer. Methods Eng.*, **20**, 1291–1306 (1984).
20. D.A. Tortorelli and R.B. Haber, 'First-order sensitivity analysis for transient conduction systems by an adjoint method', *Int. J. Numer. Methods Eng.*, **28**, 733–752 (1989).
21. D. Tortorelli, R. Haber and C.-Y. Lu, 'Design sensitivity analysis for nonlinear thermal systems', *Comput. Methods Appl. Mech. Eng.*, **77**, 61–77 (1989).
22. K. Svenningsen, J. Madsen, N.H. Hassing and W. Pauker, 'Optimization of flow geometries applying quasianalytical sensitivity analysis', *Appl. Math. Model.*, **20**, 214–224 (1996).
23. O. Baysal and M. Eleshaky, 'Aerodynamic design optimization using sensitivity analysis and computational fluid dynamics', *AIAA J.*, **30**, 718–725 (1992).
24. Z.-X. Wang, D. Tortorelli and J. Dantzig, 'Design sensitivity analysis and FEA for fluid flow with application to contraction design', *Int. J. Numer. Methods Fluids*, **23**, 991–1020 (1996).
25. M. Engleman, *FIDAP v. 7.52*, Fluid Dynamic International, Incorporated, 1996.
26. T. Morthland, P. Byrne, D. Tortorelli and J. Dantzig, 'Optimal riser design for metal castings', *Metall. Mater. Trans. B*, **26**, 871–885 (1995).
27. D. A. Tortorelli, M.M. Tiller and J.A. Dantzig, 'Optimal design of nonlinear parabolic systems—part I: Fixed spatial domain with applications to process optimization', *Comput. Methods Appl. Mech. Eng.*, **113**, 141–155 (1994).
28. R. Fox and A. McDonald, *Introduction to Fluid Mechanics*, 4th edn, Wiley, New York, 1992.
29. W. McComb, *The Physics of Fluid Turbulence*, 4th edn, Oxford University Press, New York, 1990.
30. W. Rodi, *Turbulence Models and Their Application in Hydraulics—A State of the Art Review*, University of Karlsruhe, 1980.
31. S. Patankar and D. Spalding, *Heat and Mass Transfer in Boundary Layers*, Intertext, London, 1970.
32. M. Engleman, *Fidap 7.5 Update Manual*, 1st edn, Fluid Dynamics International, Evanston, IL, 1995.
33. R. Courant, K. Friedrichs and H. Lewy, 'Über die Partiellen Differenzengleichungen der Mathematischen Physik', *Courant Inst. Math. Sci. Rep.*, **100**, 32–74 (1928).
34. O. Zienkiewicz and R. Taylor, *The Finite Element Method—Solid and Fluid Mechanics Dynamics and Non-Linearity*, vol. 2, McGraw-Hill, New York, 1991.
35. J. Reddy, *An Introduction to the Finite Element Method*, 2nd edn, McGraw-Hill, New York, 1993.
36. R. Cook, D. Malkus, and M. Plesha, *Concepts and Applications of Finite Element Analysis*, Wiley, New York, 1989.
37. R. Haftka and Z. Gurdal, *Elements of Structural Optimization*. Kluwer Academic Publishers, Netherlands, 1992.
38. D. Tortorelli, 'Design sensitivity analysis for nonlinear dynamic thermoelastic systems', *Ph.D. Thesis*, University of Illinois, Urbana-Champaign, 1988.
39. T.-M. Yao and K. Choi, '3-d shape optimal design and automatic finite regridding', *Int. J. Numer. Methods Eng.*, **28**, 369–384 (1989).
40. D. Tortorelli and Z. Wang, 'Systematic approach to shape sensitivity analysis', *Int. J. Solids Struct.*, **30**, 1181–1212 (1993).
41. A. Belegundu and S. Rajan, 'A shape optimal design and automatic finite element regridding', *Comput. Methods Appl. Mech. Eng.*, **66**, 87–106 (1988).
42. R.M. McDavid and J.A. Dantzig, 'Fluid flow in casting rigging systems: modeling, validation and optimal design', *Metall. Mater. Trans. B*, **29**, June (1998).
43. V.M.A. Engineering, *DOT Users Manual*, V.M.A. Engineering, version 3.0 ed., 1992.

